

High Frequency Land Backscatter Coefficients Over Northern Australia and the Effects of Various Surface Properties

Danielle J. Edwards¹, Manuel A. Cervera², and Andrew D. MacKinnon³

Abstract—Over-the-horizon radars (OTHRs) utilize the refractive properties of the ionosphere to illuminate targets beyond the Earth’s horizon. Consequently, the performance of this type of radar is highly dependent on the ionosphere. Reliable models of the radar ground backscatter are required to accurately assess the ionospheric propagation conditions and, thus, the expected performance of OTHR. The ground backscatter coefficient characterizes the amount of radiation scattered back from a surface toward a receiver per unit area. While the backscatter coefficient of the sea is well understood and may be calculated from theory if the sea state is known, the backscatter coefficient of land at high frequencies is not well understood. To calculate the land backscatter coefficients over Northern Australia, a methodology that compares observed backscatter ionograms to those synthesized using high-frequency (HF) radio wave ray-tracing techniques through model ionospheres was developed. Maps of the backscatter coefficients across Northern Australia were produced. The effects of surface properties, including topography, soil moisture, and vegetation cover on the backscatter coefficients, were investigated. A weak positive correlation between the backscatter coefficient and the soil moisture and surface roughness was observed; however, it was found that the vegetation had the largest effect on the backscatter coefficient.

Index Terms—Backscatter coefficient, backscatter sounder (BSS), high-frequency (HF) radar, over-the-horizon radar (OTHR).

I. INTRODUCTION

OVER-THE-HORIZON radars (OTHRs) are a class of radars that operate in the high-frequency (HF) band and are important for long-range surveillance. These radars utilize the refractive properties of the ionosphere to illuminate

targets beyond the Earth’s horizon. Consequently, their performance is highly dependent on the ionospheric propagation conditions. Backscatter sounders (BSSs) are an OTHR that measure the power returned from surface backscatter in order to assess the ionospheric propagation conditions, often for the purpose of selecting the appropriate frequency to run the main surveillance OTHR for the mission [1]. Low/high power noted by a BSS may be due to either poor/good ionospheric propagation or low/high power backscattered from the ground. Consequently, accurate models of the ground backscatter at HF are required to accurately assess the propagation conditions and, thus, the expected performance of OTHR.

The ground backscatter coefficient, otherwise known as the scattering cross section per unit area, characterizes the amount of radiation scattered back from a surface toward a receiver per unit area. While the backscatter coefficient of the sea is relatively well understood and may be calculated from theory if the sea state is known [2]–[6], the backscatter coefficient of the land at high frequencies is not well understood and is expected to be highly dependent on the terrain.

The backscatter coefficient depends on the roughness and conductivity of the surface, the polarization of the incident and scattered radio waves, the angle of incidence of the radio waves, and the radio wave frequency [7]. In order to theoretically model the backscatter coefficient of a surface, the surface properties must be characterized and the electromagnetic scattering problem must be solved. In practice, this is difficult due to many parameters of the scattering surface and the radio waves that must be known. Two main methods of doing this have been developed in the past: 1) using perturbation theory to calculate the electromagnetic properties of a surface with a specified roughness [7] and 2) constructing a surface out of objects with known scattering properties such as spheres or cylinders [8]. Studies were conducted to measure the radar cross section of trees [9] and cement walls as may be found in cities [10] for the purpose of investigating the ground backscatter coefficient. Steele [9] found that for HF backscatter, an oak tree behaves like a dipole; the radar cross section for radio waves incident at angles of elevation less than 15° was greater for vertical polarizations than horizontal polarizations. Li [11] used an OTH sky wave backscatter radar and a transponder located 1500 km from the OTH radar site with a constant output to measure the ionospheric propagation losses and the backscatter

Manuscript received 21 June 2021; revised 18 January 2022; accepted 6 February 2022. Date of publication 28 March 2022; date of current version 26 July 2022. This work was supported in part by the Defence Science and Technology Group, in part by The University of Adelaide, and in part by the Australian Government Research Training Program Scholarship. (Corresponding author: Danielle J. Edwards.)

Danielle J. Edwards was with the School of Physical Sciences, The University of Adelaide, Adelaide, SA 5005, Australia. She is now with the Defence Science and Technology Group, Edinburgh, SA 5111, Australia (e-mail: danielle.edwards@dst.defence.gov.au).

Manuel A. Cervera is with the Defence Science and Technology Group, Edinburgh, SA 5111, Australia, and also with the School of Physical Sciences, The University of Adelaide, Adelaide, SA 5005, Australia (e-mail: manuel.cervera@dst.defence.gov.au).

Andrew D. MacKinnon is with the School of Physical Sciences, The University of Adelaide, Adelaide, SA 5005, Australia (e-mail: andrew.mackinnon@adelaide.edu.au).

Color versions of one or more figures in this article are available at <https://doi.org/10.1109/TAP.2022.3161534>.

Digital Object Identifier 10.1109/TAP.2022.3161534

coefficient of a desert region and mountainous region of China. The average backscatter coefficients of these regions were found to be about -25 and -20 dB.

Methods of investigating the backscatter coefficient using oblique sounders [12] and BSSs [13], [14] have found that the backscatter coefficient is highly nonuniform with surface features, such as cities, mountains, and islands typically having greater backscatter coefficients than surrounding terrain. The differences in the backscatter coefficient of topographic features and the sea have been investigated as a way to improve the geolocation accuracy of targets via a process known as coordinate registration. This is the process of transforming from the radar (or group) range to the ground range to obtain the geographic coordinates of an object observed by a radar [15]–[18]. It has been found that the difference in the backscatter coefficient of certain topographic features could be suitable for coordinate registration.

This article describes a method of calculating backscatter coefficients using backscatter ionograms from the Jindalee Operational Radar Network (JORN) [19] in September 2015. Section II describes the data used and the method of calculating backscatter coefficients. Section III presents the backscatter coefficient results and investigates the correlation between the backscatter coefficient and various surface properties. Section IV presents the conclusions and future work.

II. MATERIALS AND METHOD

The methodology we use to calculate backscatter coefficients using backscatter ionograms is described in detail in this section. Briefly, backscatter ionograms observed by the JORN BSSs located in Northern Australia were compared with modeled backscatter ionograms, in which the backscatter coefficient was set to 0 dB. The JORN BSSs simultaneously form eight beams within a 90° area of regard to create eight backscatter ionograms. These ionograms display the power returned from radio waves that have propagated via the ionosphere and backscattered from the ground, as a function of group range and frequency. The backscatter coefficient was then calculated by taking the difference in power between the modeled and observed ionograms when all other losses were accounted for. The datasets, which characterize the soil moisture, topography, and vegetation of Northern Australia that were used to investigate the effects of various surface parameters on the backscatter coefficient (see Section III), are also described in this section.

A. Backscatter Sounder System

Backscatter ionograms recorded as part of a wider experimental trial [20] by the Longreach (LO) and Alice Springs (AS) BSSs of the JORN frequency management system (FMS) in September 2015 were used in the analysis described later in Section II-D. These ionograms had a temporal resolution of 5 min, a group range resolution of 50 km, a frequency resolution of 0.2 MHz, and a power resolution of 0.5 dBW. The JORN BSSs are a calibrated system, as described by Earl and Ward [1]. The LO and AS BSS transmit powers were notionally 15 and 10 kW, respectively. Each system monitors the actual transmitted

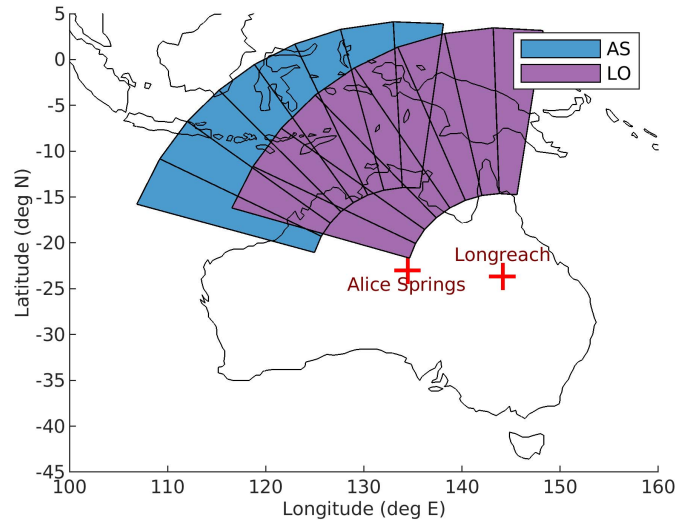


Fig. 1. BSS locations, fields of view, and disposition of the eight receive beams. The inner arcs are 1000 km from the sounders and the outer arcs are 3000 km from the sounders. The beam centers relative to bore for LO are -38.5° , -27.5° , -16.5° , -5.5° , 5.5° , 16.5° , 27.5° , and 38.5° . The beam centers relative to bore for AS are -38.2° , -26.2° , -15.4° , -5.1° , 5.1° , 15.4° , 26.2° , and 38.2° .

power as a function of frequency and scales the ionogram data to a transmit power of 20 kW.

The locations and field of view of the BSSs are shown in Fig. 1. The LO BSS transmit site is located at 23.7°S , 144.1°E and the AS BSS transmit site is located at 23.0°S , 134.5°E . Each sounder simultaneously forms eight receive beams (labeled clockwise from 1 to 8), spanning around 90° in azimuth. The BSSs operate over the frequency range 5–45 MHz. To support this large frequency range, two sets of antenna arrays (low band and high band) are used. The crossover frequency between the low and high band antennas is 32 MHz for the LO sounder and 30 MHz for the AS sounder. Each BSS transmits using a single log-periodic dipole antenna.

Reception is performed using linear arrays of 6.5 m high doublet monopoles with a doublet spacing of 3.5 m for the LO sounder [19] and a linear array of 5.5 m high dual fan monopoles with a doublet spacing of 3 m for the AS sounder [1]. Each doublet is considered a single element in the arrays. A ground mat is used for elevation control. The low band receive array for the Laverton sounder consists of 32 elements with a spacing of 6.2 m, and the high band array consists of 16 elements with a spacing of 3.7 m. The AS sounder low band array consists of 28 elements at a spacing of 6.0 m, and the high band array consists of 12 elements at a spacing of 3.9 m.

The transmit and receive antenna array gains required for the propagation loss calculations in Section II-C were modeled using Numerical Electromagnetics Code (NEC)-4 [21]. The gain patterns were generated at 0.5 MHz frequency steps at a resolution of 1.0° in elevation and 1.0° in azimuth for each of the eight beam steer angles of each sounder. These gain patterns are shown in Appendix A. Note that the surface of constant phase for a linear array has the shape of a cone. Thus, the steer azimuth, ϕ_{steer} , of the array required to receive ground scattered signals from a given ground azimuth, ϕ_{ground} ,

will vary as a function of the ray elevation, β . The relationship is given by $\sin(\phi_{\text{steer}}) = \sin(\phi_{\text{ground}}) \cos(\beta)$.

B. Real-Time Ionospheric Model

The real-time ionospheric model (RTIM) is a data-driven model, generated using data from the Australian Defence Force's network of oblique and vertical incidence sounders [22]. These sounders constantly monitor the ionosphere for the purpose of generating a near RTIM, which is required for the JORN coordinate registration system [23]. The RTIM is built from quasi-parabolic layers [24], [25] that parameterize the electron density profile. A 3-D grid of ionospheric electron densities with a temporal resolution of 5 min, and a spatial resolution of 1° in latitude and longitude and 1 km height steps was constructed from the JORN RTIM parameters for the purpose of calculating the propagation losses described in Section II-C. The coverage of the ionospheric model was from -32° to -10° in latitude, from 100° to 155° in longitude, and from 80 to 600 km in altitude. Fig. 2 shows an example of a 2-D slice through the RTIM.

C. Synthesizing Backscatter Ionograms

Model backscatter ionograms were synthesized by modeling the propagation of a fan of rays through a hindcast JORN RTIM, in a similar manner to that described by Coleman [26]. The ray-tracing toolbox PHaRLAP [27] was used to do 2-D numerical ray tracing through the model ionosphere. Fig. 2 shows an example of the ray-tracing output with the different modes of propagation labeled. Radio wave frequencies from 5 to 32 MHz with a step of 0.2 MHz were used; for each of these frequencies, a fan of rays at elevations from 2° to 50° with steps of 0.2° were ray traced.

The modeled received power P_r was calculated using a modified form of the two-way radar equation appropriate for HF propagation through the ionosphere

$$P_r = \frac{P_t G_t G_r \lambda^2 \Delta A \sigma_o}{(4\pi)^3 d_{e,o}^2 d_{e,i}^2} L_o L_i L_{pol} L_{scatt} \quad (1)$$

where P_t is the transmitted power, G_t is the transmit antenna gain, G_r is the receive antenna gain, λ is the signal wavelength, ΔA is the area of the ground illuminated by the ray, σ_o is the backscatter coefficient, $d_{e,o}$ is the out-bound effective range, $d_{e,i}$ is the in-bound effective range, L_o is the out-bound ionospheric absorption loss, L_i is the in-bound ionospheric absorption loss, L_{pol} is the polarization mismatch loss, and L_{scatt} is the forward scattering losses (which only applies for second and higher order hops) [26]. The effective range accounts for propagation effects such as ray focusing and is given by

$$d_e^2 = R_e \sin\left(\frac{D}{R_e}\right) \frac{\sin(\beta_f)}{\cos(\beta_i)} \left| \frac{dD}{d\beta_i} \right| \quad (2)$$

where β_i is the launch elevation of the ray, β_f is the ray elevation at the landing point, D is the ground range, and

R_e is the radius of the Earth [26]. The area of the ground illuminated by each ray was calculated using

$$\Delta A = R_e \sin\left(\frac{D}{R_e}\right) \left(\frac{dD}{d\beta}\right) \Delta\beta \Delta\phi \quad (3)$$

where β is the elevation angle of the transmitted ray, $\Delta\beta$ is the elevation step used in the fan of rays, and $\Delta\phi$ is the azimuthal beamwidth [13]. The azimuthal beamwidth for a linear array of antennas is given by

$$\Delta\phi = \frac{\lambda}{l \cos\theta} \quad (4)$$

where θ is the steer angle away from the bore site, λ is the wavelength of the signal, and l is the length of the receive array. It was assumed that polarization mismatch between the different polarization of the signals and the receive antenna led to a 3 dB loss in power [26].

We note that the backscatter from the surface is dependent on the polarization of the incident radiation with stronger backscatter for incident vertical polarization than horizontal polarization. However, the 2-D numerical ray tracing we have used to model the radio wave propagation does not allow us to obtain knowledge of the polarization of the incident radio waves. Furthermore, the transmitted radio waves (which are vertically polarized) will spilt into the two canonical propagation modes (the ordinary and extra-ordinary waves) when they enter the magnetized ionosphere. Due to the broad beams of the BSSs, these two elliptically polarized waves will illuminate a large area of the surface and the orientation of their electric field vectors will vary considerably over this large area. Consequently, the backscatter coefficient we calculate may be considered to be an average backscatter coefficient for each of the range–azimuth cells. This backscatter coefficient is valid when using 2-D numerical ray-tracing techniques for the interpretation of the backscatter of radio waves from other HF instruments that transmit linearly polarized radio waves.

The ionospheric absorption of radio waves consists of two components: the deviative and nondeviative absorption [28]. The nondeviative ionospheric absorption experienced by radio waves occurs mainly in the D and E layers of the ionosphere and is due to the high electron collision frequencies in this region. The George and Bradley absorption model [29], [30] was used to characterize the nondeviative absorption. The deviative absorption of the radio waves is due to appreciable amounts of deviation to their propagation path, such as at the apogee of the ray path. The George and Bradley model accounts for deviative absorption in the E layer but not in the F layer. PHaRLAP was used to account for the F layer deviative absorption in the manner described by Cervera *et al.* [31].

For the ionospheric ray tracing, the reciprocity of the in-bound and out-bound ray paths through the ionosphere was assumed and the combined out-bound and in-bound propagation paths (or modes) were found by matching the in-bound rays to the out-bound rays according to their ground range. For each out-bound ray path, there may be multiple possible in-bound ray paths. For simplicity, it was assumed that the transmit and receive sites are colocated, whereas they are in fact separated by ~ 100 km. For each propagation mode, the

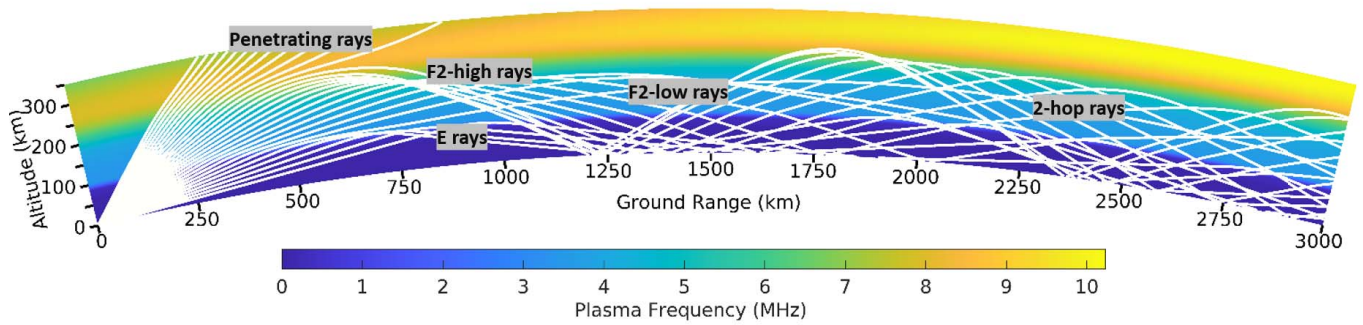


Fig. 2. Ray paths of 15 MHz radio waves through a model ionosphere computed using PHaRLAP's 2-D numerical ray-tracing engine for rays launched at various elevation angles. The model ionosphere is the JORN RTIM at 0200UT on 3/9/2015 and the origin and direction of the rays is LO beam 4.

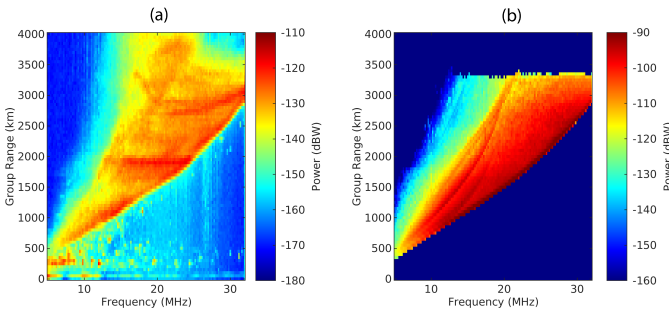


Fig. 3. Example of (a) observed and (b) modeled backscatter ionogram. The color scales are offset by 20 dB, as the losses due to the surface backscatter coefficients are not included in the modeled ionogram.

modeled received power was distributed across the group range cells encompassed, with the power contributing to each group range cell scaled appropriately. This was repeated for each of the frequencies swept over by the BSSs to populate the group range versus frequency grid of the model backscatter ionogram.

Backscatter ionograms were synthesized at around 10 min intervals using the models of the environmental conditions in September 2015 cotemporal with the observed ionograms. The ionograms were restricted to those recorded between 00:00 UT and 10:00 UT (approximately between 09:30 and 19:30 local time), as a greater range of frequencies are available for ionospheric propagation during those daytime hours. An example of a pair of observed and synthesized backscatter ionograms is shown in Fig. 3. The synthesized backscatter ionogram does not include the loss due to the ground backscatter and, thus, shows appreciably greater power.

D. Calculating the Backscatter Coefficient

The backscatter coefficient was calculated by taking the difference in power between a model and observed ionogram. An initial assessment of the suitability of the synthesized ionograms was performed to remove cases where the model did not accurately represent the ionospheric conditions. This was done by calculating the root-mean-square (rms) group range difference between the leading edges of the real and model ionograms. The leading edge is the minimum group range at which energy propagated by the ionosphere is received at each frequency. If the rms group range difference between

the leading edges was less than 300 km, the ionograms were considered similar and were retained for further analysis. The leading edge of the modeled ionograms was simple to obtain, as it was the locus of the points of the first nonzero element for each frequency in the group range versus frequency grid of the backscatter ionogram. The leading edges of the observed ionograms were obtained using a Kalman filter method. A sidelobe canceller was first applied to the backscatter ionograms to improve the ability of this algorithm to locate the leading edge. Beyond the range where E mode propagation was expected, an initial slope of the F2 mode leading edge was estimated. A Kalman filter was then used to follow this slope along the leading edge of the ionogram out to the furthest group ranges. The slope from this section of the leading edge was then used to initialize the Kalman filter to follow the downward track to the nearest group ranges and thus obtain the complete location of the leading edge of the observed ionogram.

A suitable area of the observed and modeled backscatter ionograms was then identified to calculate the backscatter coefficient. Ideally, the area of the one-hop region of a backscatter ionogram that consists of a single mode of propagation would be selected. This is desired because radio waves that have propagated via different modes may have different elevations or ground ranges, and the backscatter coefficient is expected to have an elevation and surface dependence [7]. The area of the backscatter ionogram dominated by one-hop F2-low propagation was selected as, in general, the region of the backscatter ionograms dominated by this mode was larger than any other propagation modes. This area was selected using the ray-tracing results from the model ionograms. Range–frequency cells in the one-hop region of the model ionograms where the difference between the F2-low power and the power contributed from E or F2-high propagation was less than 10 dB were removed, leaving only cells where F2-low mode propagation dominated. E propagation was defined as rays with an apogee less than 110 km and F2-high propagation was identified as those rays with a change in group range with respect to elevation greater than zero [31].

Once a suitable area was selected, the difference in power for each of the cells was calculated to yield the backscatter coefficient (see Fig. 4). The dominant propagation mode ground range, frequency, and elevation of the radio waves that contributed to each cell of the ionogram was saved

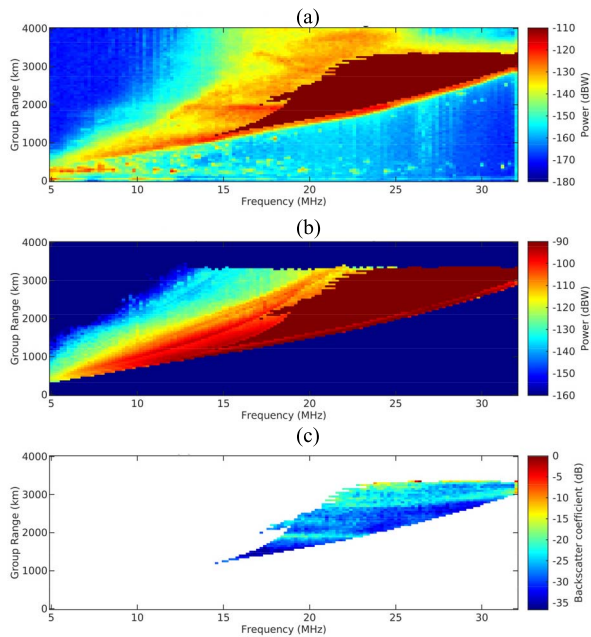


Fig. 4. (a) Observed and (b) modeled backscatter ionograms with the area deemed suitable for calculating backscatter coefficients colored in maroon. (c) Backscatter coefficient values are obtained by taking the difference in power between the modeled and observed ionograms.

for subsequent analysis, and maps of the monthly median backscatter coefficient for each range–azimuth cell viewed by the BSSs over Northern Australia were created.

E. Limitations of the Method

Variance was expected to be introduced into the backscatter coefficient results due to the limitations of the method of calculation. Differences between the JORN RTIM and the true ionospheric conditions at the time may cause errors in the modeled paths of the rays and hence in the location of the ground area that the backscatter coefficient was calculated for. The effects of errors in the ionospheric model were minimized by only using times when the shape of the modeled and observed ionograms was similar, through the use of the leading edge comparison technique described earlier. However, a balance must be struck between rejecting dissimilar ionograms and retaining enough for subsequent analysis.

The automatic selection of suitable ionograms for further analysis was dependent on finding the leading edges of the ionograms. At times, the determination of the leading edge of the observed ionograms may be erroneous due to a sidelobe response, which was not adequately removed. This could lead to otherwise suitable ionograms being removed from the analysis and decreasing the size of the dataset. In general, the leading edge comparison algorithm worked well, with 80% of the ionogram pairs considered similar.

The George and Bradley absorption model that was used to calculate the nondeviative ionospheric absorption through the lower layers of the ionosphere (the D and E layers) is a climatological model and thus does not capture day-to-day differences in the ionosphere and hence the absorption experienced by a ray. It is possible to calculate the absorption

experienced by a ray by integrating the imaginary component of the refractive index along the ray path [32], [33]. However, to calculate the ionospheric absorption in this way a model of the D layer of the ionosphere is required, which is unfortunately not included in the JORN RTIM.

The 2-D numerical ray tracing was considered adequate for this work as OTHR modeling done by Cervera *et al.* [34] found that 2-D numerical ray tracing was sufficient to characterize the performance of an OTH radar. This meant that the ray paths were limited to a plane, so out-of-plane propagation such as that introduced by a tilted ionosphere or the effect of the geomagnetic field splitting the radio waves into ordinary (O) and extraordinary (X) propagation modes could not be modeled [27]. This simplification introduces errors in the location of the region of ground backscatter, but is unexpected to be much of an issue as tilts mainly affect the azimuth of the rays and the BSS azimuth cells sizes are quite large. The 3-D numerical ray tracing would account for these effects and hence improve the accuracy to some degree; however, 3-D ray tracing is much more computationally intensive than 2-D numerical ray tracing.

Finally, an offset in the location of the one-hop F2 low region of the modeled and observed ionograms, which is within the tolerance of the leading edge check, may lead to regions being selected where other modes of propagation contributed significantly. This was minimized by reducing the size of the selected one-hop F2-low region by removing points that were near the leading and trailing edges, where the trailing edge is the maximum group range of the one-hop region at which power is received for each frequency. Points with a group range within 150 km of the modeled leading edge and 100 km of the observed leading edge were removed. Points within 2 MHz along the frequency axis of the ionogram from the group ranges of the trailing edge were also removed.

F. Investigating the Effects of Surface Properties

It was expected that the backscatter coefficient would be correlated with certain surface properties. The effects of the land topography on the backscatter coefficient were investigated using topographic data to calculate the angle of incidence of the radio waves and the roughness of the surface. The ETOPO1 Global Relief Model, accessed from the National Geophysical Data Center, NOAA [35] was used to calculate the mean surface normal of each range–azimuth bin. The angle of incidence of the radio waves was then calculated using the radio wave elevation and the mean surface normal. The rms height and the correlation length of the elevation data were used as a measure of the surface roughness. A hydrologically enforced smoothed digital elevation model (DEM-H) was accessed from Geoscience Australia [36] to calculate the rms height. The spatial resolution of this elevation data is 1 arc second (around 30 m), a similar scale size to the radio wavelengths.

Soil moisture data from the NASA National Snow and Ice Data Center [37] were used to calculate the mean soil moisture of each range–azimuth cell for comparison with the backscatter coefficient.

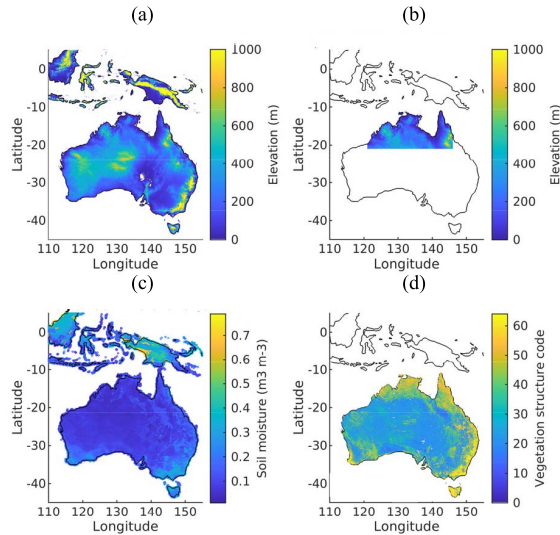


Fig. 5. Example figures of the datasets used to describe surface properties. The datasets shown are (a) ETOPO1 global relief model [35], (b) DEM-H [36], (c) Soil Moisture Active Passive (SMAP) soil moisture [37], and (d) vegetation structure codes [38]. Note that the DEM-H elevation data at locations other than that displayed are available but were not retrieved due to the large volume of this dataset.

Vegetation structure code data across Australia from 2009 were accessed from the Joint Remote Sensing and Research Project [38] (see Appendix B for a description of the vegetation structure codes). The vegetation structure code characterizes the density and height of the vegetation; larger values represent taller, denser vegetation. It was assumed that the vegetation coverage in 2015 at the spatial scales of interest had not changed significantly since 2009. The correlation between the backscatter coefficient and the angle of incidence, roughness, soil moisture, and vegetation were investigated to examine which surface properties had the largest effects. Examples of each of the datasets are shown in Fig. 5.

III. RESULTS AND DISCUSSION

A. Backscatter Coefficient Maps Over Northern Australia

Maps of the backscatter coefficient over Northern Australia were constructed to investigate how the backscatter coefficient varied across the region. The September 2015 monthly median backscatter coefficients for each range–azimuth cell viewed by the AS and LO JORN BSSs are shown in Fig. 6. It should be noted that the beamwidth is dependent on the radio wave frequency. However, for the purpose of clearly displaying these results, the beamwidth was set to a constant notional width of 11.25° . The use of a constant beamwidth is effectively displaying a nearest neighbor interpolation of the results. The number of data points contributing to each range–azimuth cell increased with range from the antenna because the one-hop F2 low mode of propagation dominated at greater ranges, and the one-hop region of the ionogram usually has a larger frequency extent at greater ranges. The mean radio wave frequency contributing to each range–azimuth cell increased with range due to the higher frequency radio waves penetrating further into the ionosphere before being refracted back to ground. The mean radio wave elevation decreased with range due to

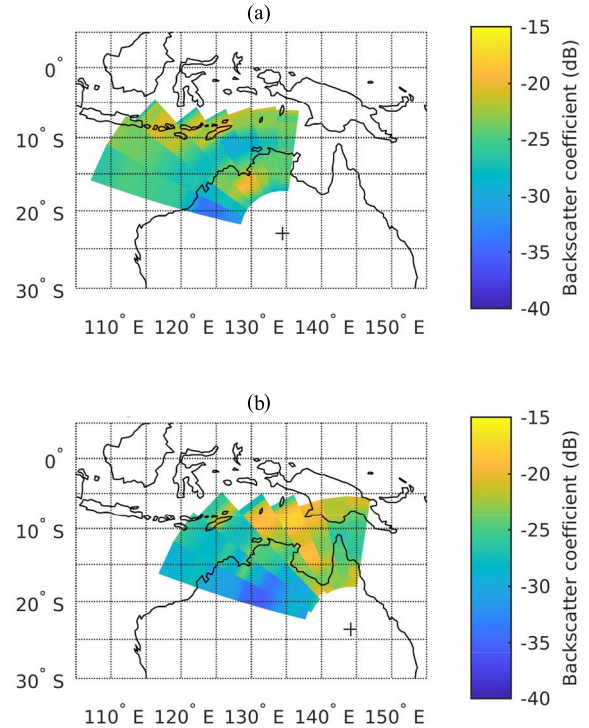


Fig. 6. Maps of the monthly median backscatter coefficient viewed by (a) AS and (b) LO BSSs in September 2015.

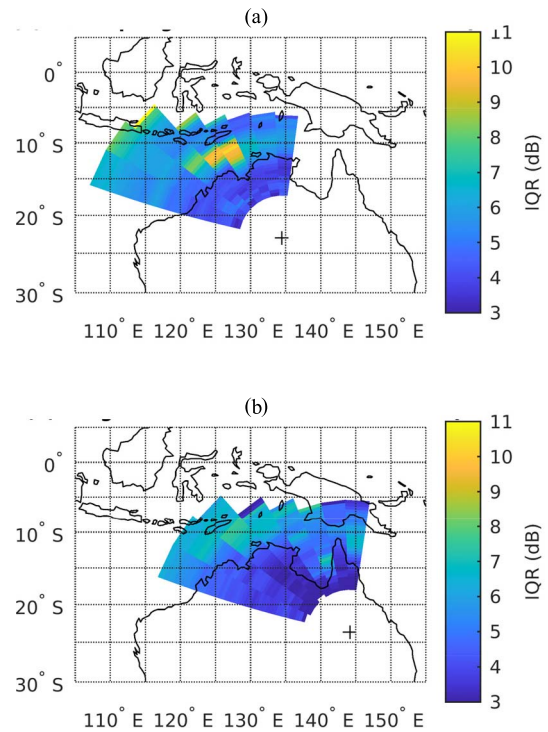


Fig. 7. IQR of the backscatter coefficient results from (a) AS and (b) LO.

the geometry of the reflections between the ground and the ionosphere.

The interquartile range (IQR) is the difference between the upper and lower quartiles and was used as a measure

of the spread in the values of the backscatter coefficient (shown in Fig. 7). There was an area of the sea between North Western Australia and Timor, which had a large IQR. This was due to large variations in the significant wave heights throughout the month in this location. The backscatter coefficient IQR from land tended to be less than that from the sea. This was expected as the land composition has little variability over the time scales of interest, unlike the sea state that has a high degree of variability associated with changes in meteorological conditions. The IQR range over the land, where the backscatter coefficient was expected to remain relatively constant, was around 3–4 dB. Over sea, the IQR was typically 6–7 dB.

Distinct regions of high and low backscatter coefficient values can be seen in the maps of the results (see Fig. 6). The lowest backscatter coefficients measured by the AS BSS occurred over the Great Sandy Desert, at around 20°S, 122°E. Similarly, the Tanami Desert in central Australia (at around 18°S, 132°E) stood out as the location where the backscatter coefficient was lowest as measured by the LO BSS. Both these locations had a backscatter coefficient of around –30 to –35 dB. These deserts are large areas of dry, relatively flat terrain with little vegetation.

Timor had a relatively large backscatter coefficient of \sim –20 dB as measured by both the AS and LO sounders. This island is dominated by large mountains running through the center and is densely vegetated. New Guinea (at around 8°S, 140–145°E) and Cairns (at around 16°S, 144°E) also stood out as areas with higher backscatter coefficients than surrounding terrain in the LO map. Again, both these regions are densely vegetated with rainforests and are mountainous. The Kimberley region in Western Australia at around 16°S, 128°E appeared as a region of higher backscatter coefficients in the AS map, but less so in the LO map, which may indicate an aspect dependence in the backscatter coefficient. The Kimberley is composed of many rough features, such as small mountain ranges and gorges.

It is expected that for a fully developed sea, where the waves have reached an equilibrium with the wind, the sea backscatter coefficient is around –23 dB [39]. This was seen over the Indian Ocean, where it is expected that the sea is fully developed. Lower sea backscatter coefficients were observed between Western Australia and Timor, while much larger backscatter coefficients were observed in the Gulf of Carpentaria (at 13°S, 139°E) and the Arafura Sea (at 8°S, 136°E). The sea backscatter coefficient was also calculated from theory using a perturbation method with a wave height spectrum calculated from sea state data [2], [4], [6]. The Joint North Sea Wave Project (JONSWAP) spectrum [40] was used with sea state data from the Centre for Australian Weather and Climate Research [41]. The backscatter coefficients calculated from this method, using a radio wave frequency of 15 MHz transmitted from AS, are shown in Fig. 8. The same trends in the backscatter coefficient, such as larger values in the Gulf of Carpentaria and the Arafura Sea and lower values between Western Australia and Timor, were seen.

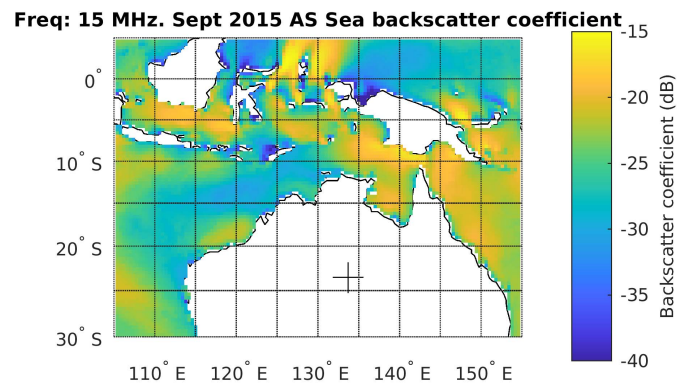


Fig. 8. Monthly daytime mean sea backscatter coefficients calculated for the AS BSS using the Barrick method in September 2015 (between 00:00 UT and 10:00 UT). A radio wave frequency of 15 MHz was used.

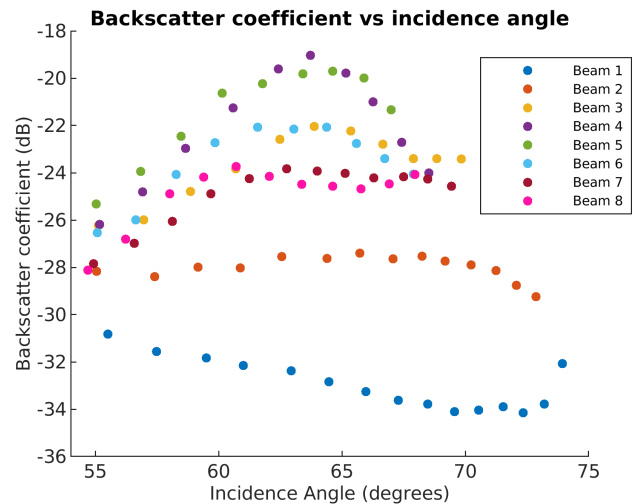


Fig. 9. Monthly median backscatter coefficient for each range–azimuth cell versus the mean angle of incidence of the radio waves reaching that cell. Different colors were used for each of the AS BSS beams.

B. Effect of the Angle of Incidence on the Backscatter Coefficient

The angle of incidence is defined as the angle between the normal to the surface and the direction of the incoming radio waves. It was expected that the backscatter coefficient would increase as the angle of incidence decreased [42], [43].

The monthly median backscatter coefficient was plotted against the mean angle of incidence for each range–azimuth cell of the eight beams from the AS BSS (see Fig. 9). The backscatter coefficient, as expected, decreased with increasing incidence angle in the beam 1 results. The majority of the land viewed by AS beam 1 is within the Great Sandy Desert, and thus, the land composition was fairly similar over all ranges. Consequently, the effects of any differences in the backscattered power due to the surface composition were reduced. However, the beam 2 results showed little variation in the backscatter coefficient with changes in the ray elevation and, furthermore, results for other beams show a maximum in the backscatter coefficient for incidence angles around 65°. This could be due to rays at lower incidence angles (closer ranges) backscattering from more desert-like areas that tend to

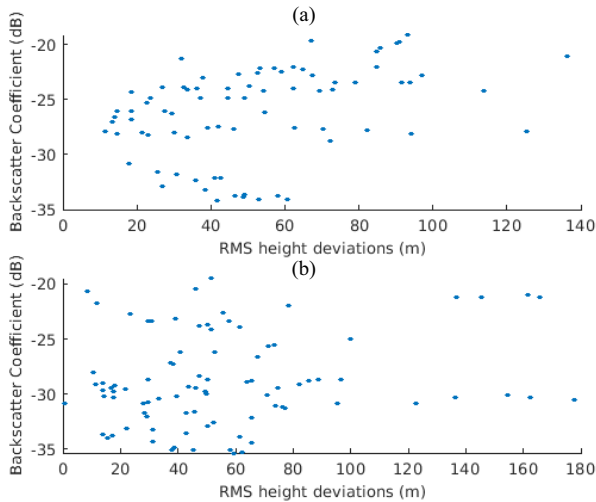


Fig. 10. September 2015 monthly median backscatter coefficient versus the roughness of each range–azimuth cell from (a) AS and (b) LO.

have low backscatter coefficients, whereas the high incidence angle rays reach the highly vegetated regions of Northern Australia. In general, the expected trend of the backscatter coefficient decreasing with angle of incidence was not found. This was likely due to other parameters that also affect the backscatter coefficient obscuring this relationship. Similarly, it was difficult to draw conclusions on the relationship between the backscatter coefficients and the angle of incidence for the LO results.

C. Effect of the Surface Roughness on the Backscatter Coefficient

In the context of radio waves scattering from a surface, the roughness of a surface is dependent on the wavelength of the incident radio waves; a surface is considered rough if features of that surface are on the same scale or larger than the wavelength of the radio waves. The type of scattering from a surface depends on the roughness of that surface, as specular scattering dominates for a very rough surface, while diffuse scattering dominates when a surface is slightly rough [7]. Here, a slightly rough surface is defined as $k_0\zeta \cos \theta_i < 1.0$ and a very rough surface is defined as $k_0\zeta \cos \theta_i > 1.0$, where k_0 is the signal wavenumber, ζ is the mean height of surface variations, and θ_i is the angle of incidence of the signal from the mean surface normal.

The backscatter coefficient was plotted against the rms height of the DEM-H elevation data for each range–azimuth cell (shown in Fig. 10) and a Pearson linear correlation test was conducted on the results. This tested the null hypothesis that there was no relationship between the parameters. The strength of the correlation was represented by the absolute value of the correlation coefficient and the direction was represented by the sign of the correlation coefficient. The significance level was given by the p-value. The correlation coefficients for the AS and LO results were 0.38 and 0.20, respectively, with p-values of <0.001 and 0.067. These results suggest a weak but statistically significant correlation between the backscatter coefficient and surface roughness for the area viewed by the

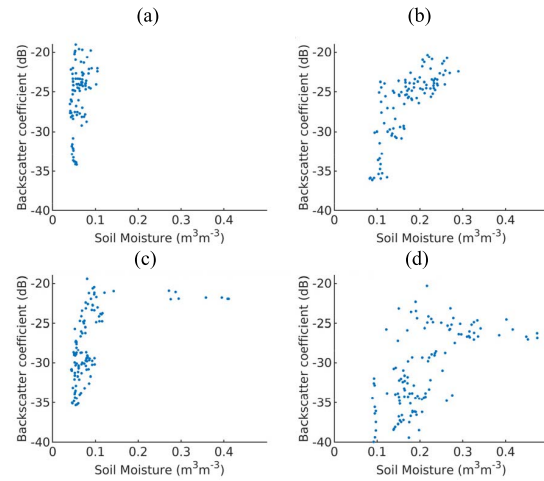


Fig. 11. Plots of the monthly median backscatter coefficient versus the mean soil moisture for (a) AS September 2015, (b) AS March 2016, (c) LO September 2015, and (d) LO March 2016.

AS sounder. However, for the LO results, the p-value indicates that the null hypothesis of no correlation cannot be rejected at the 95% confidence level. Mainland Australia is relatively flat; there are no great mountain ranges or other features in the areas observed that could cause large rms height deviations. This limited range of roughness values may be one reason why little correlation was seen between the rms height deviation and the backscatter coefficient.

The correlation length of the surface was also used to parameterize the surface roughness. A slice of the surface elevation data in the direction of the maximum beam gain was used to calculate the correlation length for each range cell. A Pearson correlation test was conducted to investigate the relationship between the backscatter coefficient and the surface correlation length. The results from this test were not statistically significant. Correlation coefficients of -0.44 and -0.49 were found for AS and LO, respectively. The corresponding p-values were 0.31 and 0.10 for AS and LO, respectively.

D. Effect of the Soil Moisture on the Backscatter Coefficient

Changes in soil moisture affect the conductivity and relative permittivity of the land. As the soil moisture increases, the soil becomes more conductive and this affects the radio wave reflectivity of the surface. A surface with an increased conductivity will reflect a greater amount of energy from the incident radio waves [44]. Hence, it was expected that an increase in the soil moisture would increase the backscatter coefficient. Since September is during the Northern Australian dry season, backscatter coefficients were also calculated for March 2016. March is at the end of the Northern Australian wet season, so there was a considerable amount of rainfall during this month.

Plots of the monthly median backscatter coefficient versus the mean soil moisture for each range–azimuth cell of both the sounders in September 2015 and March 2016 are shown in Fig. 11. A Pearson linear correlation test was conducted to test the null hypothesis that the backscatter coefficient and

the soil moisture were not related. During September, the correlation coefficients were 0.39 and 0.53 for AS and LO, respectively, both with p-values of <0.001 . During March, the correlation coefficients were 0.76 and 0.63 for AS and LO, respectively, again both with p-values of <0.001 . The correlation coefficients were significant at the 99% confidence level and showed that there was a weak-to-moderate positive correlation in the September results and a stronger positive correlation in the March results.

The range of backscatter coefficient values for these two months was similar (especially for AS), but the range of soil moisture values was much larger in March. This suggests that the soil moisture may not change the backscatter coefficient appreciably, but these locations, which experience increased soil moisture during the year, also have other properties that may cause the backscatter coefficient to be larger. For example, an area that consistently experiences larger amounts of rainfall during the year may also experience more erosion over many years causing gorges and other topographic features that would increase the surface roughness or increased soil moisture in an area could provide better conditions for vegetation to grow, which may also affect the backscatter coefficient.

The soil moisture varied throughout the month due to the appreciable but variable amount of rainfall during March 2016. Consequently, we decided to investigate how changes in the soil moisture affected the backscatter coefficient at a single location, thereby reducing the impact of other surface variables on the results. For each range–azimuth cell, the mean soil moisture and 3 h median backscatter coefficient was calculated at three times (01:30 UT, 04:30 UT, and 07:30 UT) for each day of the month. A Pearson correlation test was then conducted for each range–azimuth cell, testing the null hypothesis that there was no relationship between the backscatter coefficient and the soil moisture throughout March. A histogram of the correlation coefficients for all of the AS and LO range–azimuth cells in March 2016 is shown in Fig. 12. The median correlation coefficient was 0.13, which indicates that the backscatter coefficient has a weak relationship with the soil moisture. The p-value was greater than 0.05 for 82% of the range–azimuth cells. Hence, the null hypothesis that there was no correlation between the soil moisture and the backscatter coefficient was unable to be rejected for most of the range–azimuth cells. However, changes in the soil moisture throughout the month within each range–azimuth cell were not large despite the overall variable amount of rainfall. The median of the spread in the soil moisture values (the difference between the maximum and minimum moisture values for a given range–azimuth cell) for all the AS and LO range–azimuth cells during March 2016 was low at $0.13 \text{ m}^3/\text{m}^3$. The low variability in the moisture content of each individual ground range–azimuth cell means that it is difficult to draw any conclusions from Fig. 12.

E. Effect of the Vegetation on the Backscatter Coefficient

It was suggested by Steele [9] that trees may act as dipoles, absorbing and reradiating HF signals back toward a receive antenna. From the vegetation data, most of the trees

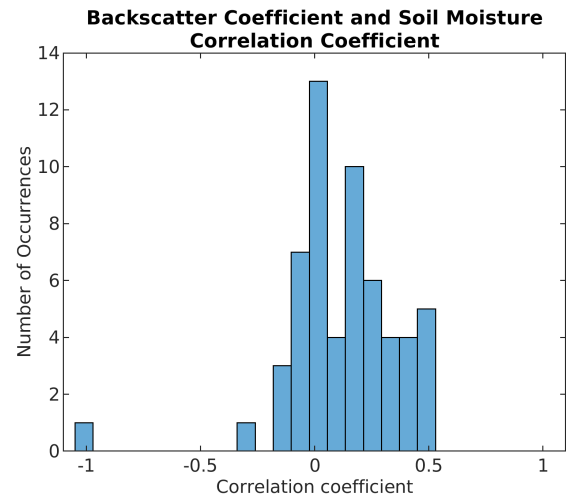


Fig. 12. Histogram of Pearson correlation coefficients testing the correlation between the backscatter coefficient and soil moisture using both the AS and LO March 2016 data. The median correlation coefficient is 0.13.

Backscatter Coefficient vs. Vegetation (September 2015)

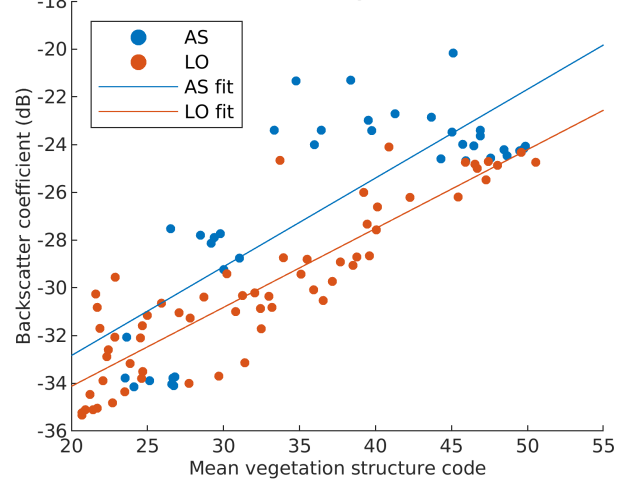


Fig. 13. Plot of the monthly median backscatter coefficient for each range–azimuth cell versus the mean vegetation code for that cell using the AS (blue) and LO (orange) results. Lines of best fit were fitted using linear regression.

had heights of the order of half to a full radar wavelength (10–30 m) and thus would be near the resonance length of integer multiples of a half wavelength. A plot of the monthly median backscatter coefficient versus the mean vegetation structure code for each range azimuth cell is shown in Fig. 13. A Pearson linear correlation test was conducted to test the null hypothesis that there was no relationship between the backscatter coefficient and the vegetation structure code. The correlation coefficients of 0.79 and 0.88 were obtained for the AS and LO results, respectively, with a p-value of <0.001 for both. This test showed that there was a strong positive correlation between the backscatter coefficient and the vegetation structure, and this correlation was significant at the 99% confidence level. Lines of best fit were fitted to the results using linear regression. The slopes of the fitted lines were 0.37 ± 0.05 and 0.33 ± 0.02 for AS and LO, respectively. The intercepts of the fitted lines were -40.3 ± 1.8 and $-40.7 \pm 0.7 \text{ dB}$ for AS and LO, respectively. Within the

standard error of the fit, the AS and LO results are in agreement.

A closer inspection of the AS results indicates that the relationship between the vegetation and backscatter coefficient flattens out once a vegetation structure code of around 35 is reached. However, with the LO results, the backscatter coefficient increased with increasing vegetation through to the maximum vegetation code observed of 53. This difference in behavior may be due to the way in which the vegetation structure code is defined; codes of 31–33 imply a coverage of 6%–11%, codes of 41–44 imply a coverage of 11%–30%, and codes from 51–53 imply a coverage of 30%–70%. Values between these codes were created through the process of averaging the vegetation code data within each region. Since there are large ranges in the fraction of coverage for a single vegetation code, it may be that regions with codes from 35 to 50 in the AS results had a similar fraction of vegetation coverage, whereas in the LO results, there could be a larger range of vegetation coverage values. Regions with a vegetation code >50 were in the LO sounder field of regard, but not the AS sounder. As the AS sounder was located in central Australia, all regions close to the sounder had little vegetation, while the regions further away had much more vegetation. There was not a variety of different vegetation structures at similar ranges from the sounder. In contrast, the LO sounder field of regard covered regions of different levels of vegetation at many different ranges. This means that the LO sounder is more favorably located for investigating the relationship between the vegetation and the backscatter coefficient, as the effects on the backscatter coefficient due to different frequencies and elevations associated with different ranges should be smoothed out.

The correlation between the backscatter coefficient and the vegetation density that was observed is not necessarily due to vegetation alone; as discussed earlier, it may be due to areas with dense vegetation also having increased soil moisture or being mountainous or rough in nature. However, due to the little impact seen on the backscatter coefficient from soil moisture or roughness as shown in Sections III-C and III-D, it appears likely that the increase in the backscatter coefficient with vegetation structure code was mostly due to the vegetation.

IV. CONCLUSION

A model of ground backscatter coefficients is important for assessing the performance of OTHRs. A method for calculating backscatter coefficients by comparing observed backscatter ionograms to synthesized backscatter ionograms where all other losses were accounted for was developed. Maps of the backscatter coefficients over Northern Australia when observed by the AS and LO JORN BSSs were produced. In these maps, topographic features, such as desert regions and mountain ranges, could be identified along with land/sea transitions. Deserts had lower backscatter coefficients of around -30 to -35 dB, while tropical, densely vegetated regions had backscatter coefficients of up to around -20 dB. The effects of various surface parameters on the backscatter

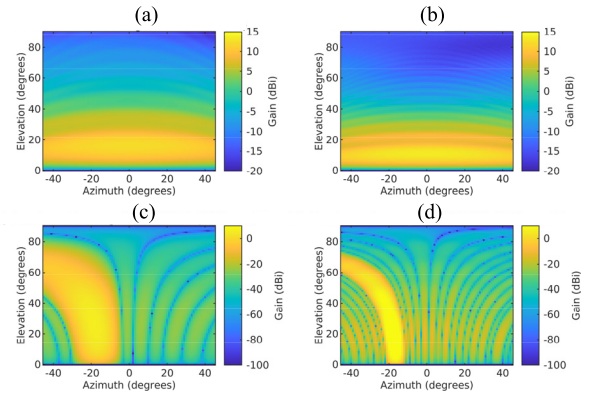


Fig. 14. Transmit antenna gain for a JORN sounder at (a) 10 and (b) 25 MHz. Receive antenna gain for Beam 3 of a JORN sounder (steered -16.5° off boresight) at (c) 10 and (d) 25 MHz.

coefficient were investigated. A weak positive correlation between the backscatter coefficient and the surface roughness and soil moisture was observed. However, it was found that the backscatter coefficient was highly correlated with the vegetation structure. The backscatter coefficient increased with increasing vegetation density and height, which may be explained by the trees acting similar to antennas, absorbing and reradiating the energy back toward the receiver.

To further understand how the backscatter coefficient changes over time and how changes in the surface parameters affect the backscatter coefficient, a study over a longer period of time needs to be conducted. Backscatter ionograms observed over a decade could be used to investigate seasonal trends in the backscatter coefficient. Future experiments using higher spatial resolution data would allow the dependence of the backscatter coefficient on surface properties to be investigated in more detail.

APPENDIX

A. Antenna Gain Patterns

The antenna patterns were calculated using a method-of-moments electromagnetic solver, NEC [21]. The transmit antenna gains and the receive gains, including the power loss due to antenna impedance mismatch, were used for the given direction and frequencies required for each of the beams. The transmit antenna gain for a JORN sounder at 10 and 25 MHz is shown in Fig. 14(a) and (b), respectively. The receive antenna gain for a JORN sounder steered toward beam 3 at 10 and 25 MHz is shown in Fig. 14(c) and (d), respectively.

B. Vegetation Height and Structure Data

A map of the vegetation height and structure across Australia (see Fig. 15) was used to investigate the correlation between the backscatter coefficient and the vegetation. This was accessed from the Joint Remote Sensing and Research Project [38]. The data contained forest structure codes, which are dependent on the plant coverage and height (see Table I) and covered latitudes from -6° to -45° and longitudes from 108° to 160° , with a spatial resolution of 30 m. A 30 m spatial resolution was much finer than required for this work, so the

TABLE I
DEFINITION OF THE FOREST STRUCTURE CODES [38]

Code	Structural Formation	Total cover (%)	plant fraction	95th Percentile Height (m)
0	No Data	-	-	-
10	No trees	0	-	-
21	Low scattered trees	0 to 6	< 9	< 9
22	Medium scattered trees	0 to 6	9 to 17	9 to 17
31	Low open woodland	6 to 11	< 9	< 9
32	Medium open woodland	6 to 11	9 to 17	9 to 17
33	Tall open woodland	6 to 11	17 to 27	17 to 27
41	Low woodland	11 to 30	< 9	< 9
42	Medium woodland	11 to 30	9 to 17	9 to 17
43	Tall woodland	11 to 30	17 to 27	17 to 27
44	Very tall woodland	11 to 30	27 to 57	27 to 57
51	Low open forest	30 to 70	< 9	< 9
52	Medium open forest	30 to 70	9 to 17	9 to 17
53	Tall open forest	30 to 70	17 to 27	17 to 27
54	Very tall open forest	30 to 70	27 to 57	27 to 57
55	Extremely tall open forest	30 to 70	> 57	> 57
63	Tall closed forest	> 70	17 to 27	17 to 27
64	Very tall closed forest	> 70	27 to 57	27 to 57

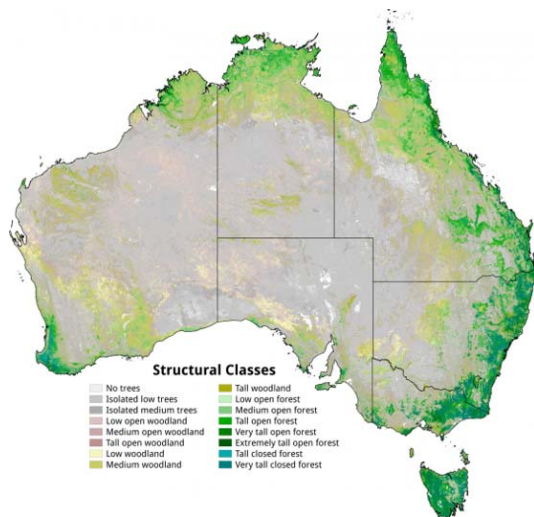


Fig. 15. Vegetation structural classes across Australia. Image from [38].

data were decimated in both directions, resulting in a decrease in size by a factor of 100. The vegetation data obtained were for a single snapshot of the vegetation coverage of Australia in 2009. However, it was assumed that the vegetation structure at the spatial scales of interest had not changed significantly, so it was used to compare the backscatter coefficients calculated for 2015 and 2016.

ACKNOWLEDGMENT

The authors acknowledge Prof. Trevor Harris, Dr. David Netherway, and Prof. David Holdsworth for useful discussions and suggestions.

Results were obtained using the HF propagation toolbox, PHaRLAP, developed by the Defence Science and Technology Group, Australia. This toolbox is available from <https://www.dst.defence.gov.au/opportunity/pharlap-provision-high-frequency-raytracing-laboratory-propagation-studies>.

BSS data and RTIM data are owned by the Australian Commonwealth Government, Department of Defence.

They may be made available on a case-by-case basis pursuant to the Defence Science and Technology Group policy for public release of information by contacting the primary author. Other datasets used for this research are available in these in-text data citation references: Amante and Eakins [35], NOAA National Geophysical Data Center [45] [Creative Commons Attribution 4.0 International License], Durrant *et al.* [41] [Creative Commons Attribution-ShareAlike 4.0 International License], Gallant *et al.* [36] [Creative Commons Attribution 4.0 International License], Reichle *et al.* [37], and Scarth *et al.* [38] [Creative Commons Attribution (CC-BY) 4.0 International License].

REFERENCES

- [1] G. F. Earl and B. D. Ward, "The frequency management system of the Jindalee over-the-horizon backscatter HF radar," *Radio Sci.*, vol. 22, no. 2, pp. 275–291, Mar. 1987.
- [2] D. Barrick, "First-order theory and analysis of MF/HF/VHF scatter from the sea," *IEEE Trans. Antennas Propag.*, vol. AP-20, no. 1, pp. 2–10, Jan. 1972.
- [3] B. Lipa, B. Nyden, D. Barrick, and J. Kohut, "HF radar sea-echo from shallow water," *Sensors*, vol. 8, no. 8, pp. 4611–4635, 2008.
- [4] B. J. Lipa and D. E. Barrick, "Extraction of sea state from HF radar sea echo: Mathematical theory and modeling," *Radio Sci.*, vol. 21, no. 1, pp. 81–100, Jan./Feb. 1986.
- [5] C. Neller, "Over-the-horizon radar sea-state parameter estimation using bureau of meteorology interactive weather and wave forecast data," NSID, DST Group, Edinburgh, SA, Australia Tech. Rep., DSTO-DP-1266, 2014.
- [6] D. E. Barrick, J. M. Headrick, R. W. Bogle, and D. D. Crombie, "Sea backscatter at HF: Interpretation and utilization of the echo," *Proc. IEEE*, vol. 62, no. 6, pp. 673–680, Jun. 1974.
- [7] D. E. Barrick and W. H. Peake, "A review of scattering from surfaces with different roughness scales," *Radio Sci.*, vol. 3, no. 8, pp. 865–868, Aug. 1968.
- [8] W. Peake, "Theory of radar return from terrain," in *Proc. IRE Int. Conv. Rec.*, New York, NY, USA, Mar. 1966, pp. 27–41.
- [9] J. G. Steele, "High-frequency backscatter from terrain with trees," *Proc. IEEE*, vol. 55, no. 9, pp. 1583–1590, Sep. 1967.
- [10] J. R. Barnum, "High-frequency backscatter from terrain with cement-block walls," *IEEE Trans. Antennas Propag.*, vol. AP-19, no. 3, pp. 343–347, May 1971.
- [11] L.-W. Li, "High-frequency over-the-horizon radar and ionospheric backscatter studies in China," *Radio Sci.*, vol. 33, no. 5, pp. 1445–1458, Sep./Oct. 1998.
- [12] R. P. Basler and T. D. Scott, "Ground backscatter observed with high resolution oblique sounders," *Radio Sci.*, vol. 7, no. 2, pp. 239–243, Feb. 1972.
- [13] B. Slimming and M. Cervera, "Calculation of high frequency land backscatter coefficients," NSID, DST Group, Edinburgh, SA, Australia, Tech. Rep., Group-TR-3613, 2019, [Online]. Available: <https://www.dst.defence.gov.au/sites/default/files/publications/documents/DST-Group-TR-3613.pdf>
- [14] D. J. Edwards, "High frequency surface backscatter coefficients," M.Phil. thesis, Dept. Physics, School Phys. Sci., Univ. Adelaide, Adelaide, SA, Australia, 2020.
- [15] D. A. Holdsworth, "Skywave over-the-horizon radar track registration using Earth surface and infrastructure backscatter," in *Proc. IEEE Radar Conf. (RadarConf)*, Seattle, WA, USA, May 2017, pp. 0986–0991.
- [16] J. R. Barnum and E. E. Simpson, "Over-the-horizon radar target registration improvement by terrain feature localization," *Radio Sci.*, vol. 33, no. 4, pp. 1077–1093, Jul. 1998.
- [17] M. D. E. Turley, R. S. Gardiner-Garden, and D. A. Holdsworth, "High-resolution wide area remote sensing for HF radar track registration," in *Proc. Int. Conf. Radar*, Adelaide, SA, Australia, Sep. 2013, pp. 128–133.
- [18] Z. Jin, Q. Pan, C. Zhao, and W. Zhou, "SVM based land/sea clutter classification algorithm," *Appl. Mech. Mater.*, vol. 236, pp. 1156–1162, Nov. 2012.
- [19] A. Cameron, "The Jindalee operational radar network: Its architecture and surveillance capability," in *Proc. Int. Radar Conf.*, Alexandria, VA, USA, 1995, pp. 692–697.

- [20] R. Gardiner-Garden *et al.*, "A description of the elevation sensitive oblique incidence sounder experiment (ELOISE)," *Adv. Space Res.*, vol. 64, no. 10, pp. 1887–1914, Nov. 2019.
- [21] G. Burke, A. Poggio, J. Logan, and J. Rockway, "NEC—Numerical electromagnetics code for antennas and scattering," in *Proc. Antennas Propag. Soc. Int. Symp.*, Seattle, WA, USA, Jun. 1979, pp. 147–150.
- [22] R. Barnes, R. Gardiner-Garden, and T. Harris, "Real time ionospheric models for the Australian Defence Force," in *Proc. WARS*, 2000, Art. no. 122135.
- [23] T. J. Harris, A. D. Quinn, and L. H. Pederick, "The DST group ionospheric sounder replacement for JORN," *Radio Sci.*, vol. 51, no. 6, pp. 563–572, Jun. 2016.
- [24] P. L. Dyson and J. A. Bennett, "A model of the vertical distribution of the electron concentration in the ionosphere and its application to oblique propagation studies," *J. Atmos. Terr. Phys.*, vol. 50, no. 3, pp. 251–262, 1988.
- [25] R. I. Barnes, S. A. Braendler, C. J. Coleman, R. S. Gardiner-Garden, and T. V. Hoang, "Analysis of data-driven parametric models of the vertical ionospheric profile for use in oblique propagation studies," *Radio Sci.*, vol. 33, no. 4, pp. 1215–1226, Jul. 1998.
- [26] C. J. Coleman, "On the simulation of backscatter ionograms," *J. Atmos. Sol.-Terr. Phys.*, vol. 59, no. 16, pp. 2089–2099, 1997.
- [27] M. A. Cervera and T. J. Harris, "Modeling ionospheric disturbance features in quasi-vertically incident ionograms using 3-D magnetoionic ray tracing and atmospheric gravity waves," *J. Geophys. Res., Space Phys.*, vol. 119, no. 1, pp. 431–440, Jan. 2014.
- [28] K. Davies, *Ionospheric Radio*. London, U.K.: IET, 2008.
- [29] P. L. George and P. A. Bradley, "Relationship between H.F. Absorption at vertical and oblique incidence," *Proc. Inst. Elect. Eng.*, vol. 120, no. 11, pp. 1355–1361, 1973.
- [30] P. L. George and P. A. Bradley, "A new method of predicting the ionospheric absorption of high frequency waves at oblique incidence," *ITU Telecommun. J.*, vol. 41, pp. 307–312, May 1974.
- [31] M. A. Cervera, T. J. Harris, D. A. Holdsworth, and D. N. Netherway, "Ionospheric effects on HF radio wave propagation," in *Space Physics and Aeronomy, Ionosphere Dynamics and Applications* (Geophysical Monograph), vol. 3. Hoboken, NJ, USA: Wiley, 2021.
- [32] L. H. Pederick and M. A. Cervera, "Semiempirical model for ionospheric absorption based on the NRLMSISE-00 atmospheric model," *Radio Sci.*, vol. 49, no. 2, pp. 81–93, Feb. 2014.
- [33] K. A. Zawdie, D. P. Drob, D. E. Siskind, and C. Coker, "Calculating the absorption of HF radio waves in the ionosphere," *Radio Sci.*, vol. 52, no. 6, pp. 767–783, 2017.
- [34] M. A. Cervera, D. B. Francis, and G. J. Frazer, "Climatological model of over-the-horizon radar," *Radio Sci.*, vol. 53, no. 9, pp. 988–1001, Sep. 2018.
- [35] C. Amante and B. W. Eakins, "ETOPO1 1 arc-minute global relief model: Procedures, data sources and analysis," Nat. Geophys. Data Center, NOAA, Washington, DC, USA, Tech. Rep., NESDIS NGDC-24, 2009.
- [36] J. Gallant, N. Wilson, T. Dowling, A. Read, and C. Inskip, "SRTM-derived 1 second digital elevation models version 1.0. dataset," Geosci. Aust., Canberra, ACT, Australia, 2011. [Online]. Available: <http://pid.geoscience.gov.au/dataset/ga/72759>
- [37] R. Reichle, G. De Lannoy, R. D. Koster, W. T. Crow, J. S. Kimball, and Q. Liu, "SMAP L4 global 3-hourly 9 km EASE-grid surface and root zone soil moisture geophysical data, version 4," NASA Nat. Snow Ice Data Center Distrib. Act. Arch. Center, Boulder, CO, USA, 2018, doi: [10.5067/KPJNN2GH1DQR](https://doi.org/10.5067/KPJNN2GH1DQR).
- [38] P. Scarth, J. Armston, R. Lucas, and P. Bunting, "A structural classification of Australian vegetation using ICESat/GLAS, ALOS PALSAR, and Landsat sensor data," *Remote Sens.*, vol. 11, no. 2, p. 147, Jan. 2019.
- [39] W. H. Munk and W. A. Nierenberg, "High frequency radar sea return and the Phillips saturation constant," *Nature*, vol. 224, no. 5226, p. 1285, 1969.
- [40] K. Hasselmann *et al.*, "Measurements of wind-wave growth and swell decay during the joint North Sea Wave project (JONSWAP)," *Deut. Hydrogr. Z.*, vol. 8, pp. 1–95, Jan. 1973.
- [41] T. H. Durrant, D. J. M. Greenslade, M. A. Hemer, and C. E. Trenham, "A global wave hindcast focussed on the Central and South Pacific," Centre Austral. Weather Climate Res., VIC, Australia, Tech. Rep. 070, 2014.
- [42] F. T. Ulaby, P. P. Batlivala, and M. C. Dobson, "Microwave backscatter dependence on surface roughness, soil moisture, and soil texture: Part I-bare soil," *IEEE Trans. Geosci. Electron.*, vol. GE-16, no. 4, pp. 286–295, Oct. 1978.
- [43] D. Barrick, "Grazing behavior of scatter and propagation above any rough surface," *IEEE Trans. Antennas Propag.*, vol. 46, no. 1, pp. 73–83, Jan. 1998.
- [44] J. D. Jackson, *Classical Electrodynamics*, 2nd ed. New York, NY, USA: Wiley, 1975.
- [45] *ETOPO1 1 Arc-Minute Global Relief Model*, NOAA Nat. Centers Environ. Inf., NOAA Nat. Geophys. Data Center, Boulder, CO, USA, 2009.



Danielle J. Edwards received the B.Sc. degree in experimental and theoretical physics and the M.Phil. degree in physics from The University of Adelaide, Adelaide, SA, Australia, in 2018 and 2021, respectively.

Since 2019, she has been a Physicist with the High Frequency Systems Group, Defence Science and Technology Group, Edinburgh, SA, Australia. Her research interests include ionospheric physics, the propagation of high-frequency radio waves, and performance modeling of over-the-horizon radar.



Manuel A. Cervera received the B.Sc. (Hons.) and Ph.D. degrees from the Physics Department, The University of Adelaide, Adelaide, SA, Australia, in 1990 and 1996, respectively.

Since 2018, he has been an Adjunct Associate Professor with the Space and Atmospheric Physics Group, School of Physical Sciences, The University of Adelaide. He is also a Senior Scientist and the Discipline Leader for radar performance and environment in the HF systems science and technology capability area at the Defence Science and Technology Group, Edinburgh, SA, Australia. His research interests include ionospheric physics, radio wave propagation through the ionosphere, HF radio systems, and performance modeling of over-the-horizon radar.



Andrew D. MacKinnon received the Ph.D. degree in physics from The University of Adelaide, Adelaide, SA, Australia, in 2001.

After his Ph.D. degree, he was a Post-Doctoral Fellow with The University of Adelaide. He then took up a position of a Research Scientist at Atmospheric Radar Systems, Thebarton, SA, Australia, in 2003. In 2004, he returned to The University of Adelaide, where he became a Senior Research Associate in 2008. In 2009, he accepted a position as a Lecturer and became the Inaugural First Year Director of physics in 2011. In 2016, he was one of the inaugural members of the University of Adelaide Education Academy, Adelaide. Since 2019, he has been the Head of the Physics Department, The University of Adelaide. Despite being an education-focused specialist, he has maintained his research interest by being an active member of the Space and Atmospheric Physics Group, The University of Adelaide, supervising postgraduate students.

Dr. MacKinnon is a member of the Australian Institute of Physics. He was on the South Australian Committee from 2015 to 2020 and the Chair from 2017 to 2018.